



# X-ray absorption spectroscopy characterization of embedded and extracted nano-oxides



Tiberiu Stan <sup>a,\*</sup>, David J. Sprouster <sup>b</sup>, Avishai Ofan <sup>b</sup>, G. Robert Odette <sup>a</sup>, Lynne E. Ecker <sup>b</sup>, Indrajit Charit <sup>c</sup>

<sup>a</sup> Materials Department, University of California Santa Barbara, Santa Barbara, CA, 93106, USA

<sup>b</sup> Nuclear Science and Technology Department, Brookhaven National Laboratory, Upton, NY, 11973, USA

<sup>c</sup> Chemical and Materials Engineering Department, University of Idaho, Moscow, ID, 83844, USA

## ARTICLE INFO

### Article history:

Received 7 October 2016

Received in revised form

13 December 2016

Accepted 27 December 2016

Available online 29 December 2016

### Keywords:

Nanostructured materials

Nuclear reactor materials

Synchrotron radiation

EXAFS

## ABSTRACT

The chemistries and structures of both embedded and extracted Y–Ti–O nanometer-scale oxides in a nanostructured ferritic alloy (NFA) were probed by x-ray absorption spectroscopy (XAS). Y<sub>2</sub>Ti<sub>2</sub>O<sub>7</sub> is the primary embedded phase, while the slightly larger extracted oxides are primarily Y<sub>2</sub>TiO<sub>5</sub>. Analysis of the embedded nano-oxides is difficult partly due to the multiple Ti environments associated with different oxides and those still residing in matrix lattice sites. Thus, bulk extraction followed by selective filtration was used to isolate the larger Y<sub>2</sub>TiO<sub>5</sub> oxides for XAS, while the smaller predominant embedded phase Y<sub>2</sub>Ti<sub>2</sub>O<sub>7</sub> oxides passed through the filters and were analyzed using the log-ratio method.

© 2017 Elsevier B.V. All rights reserved.

## 1. Introduction

Nanostructured ferritic alloys (NFAs) are a developmental class of oxide dispersion strengthened steels (ODS) with potential applications in nuclear fission and fusion energy systems. NFAs are thermally stable, have excellent high-temperature creep strength and are uniquely irradiation tolerant [1–4]. NFAs are typically processed by ball-milling Fe–14Cr–W–Ti metallic powders with yttria (Y<sub>2</sub>O<sub>3</sub>) powders followed by hot consolidation leading to the precipitation of Y–Ti–O nano-oxides (NOs) that impede dislocation motion, enhance defect recombination and trap transmutation produced He in small high-pressure gas bubbles [1,2].

Some of the major challenges facing NFAs include characterization of the NO sizes, number densities, structures, compositions, and oxide-matrix interfaces. These characteristics depend on the alloy composition and processing history. NO characterization is complicated by the presence of many precipitate phases that range from one to hundreds of nanometers. Further, the various methods used to characterize NOs do not always yield the same results.

\* Corresponding author. Materials Department, University of California Santa Barbara, Santa Barbara, CA, 93117, USA.

E-mail address: [tstan@engineering.ucsb.edu](mailto:tstan@engineering.ucsb.edu) (T. Stan).

Studies have been interpreted to show NOs that range from solute enriched clusters with core-shell structures to various complex oxides, such as fcc Y<sub>2</sub>Ti<sub>2</sub>O<sub>7</sub> and orthorhombic Y<sub>2</sub>TiO<sub>5</sub>. Some atom probe tomography (APT) studies suggest NOs are non-stoichiometric Guinier-Preston zone-like phases with high Ti/Y ratios [5–9]. However, most transmission electron microscopy (TEM) [10–16] and small angle neutron and x-ray scattering (SANS and SAXS) [13,17,18] studies report structures and chemistries that are primarily consistent with the fcc pyrochlore Y<sub>2</sub>Ti<sub>2</sub>O<sub>7</sub> phase.

Previous TEM and SANS studies on reference NFA MA957 indicate NO averages for number densities of  $N \sim 5 \times 10^{23} \text{ m}^{-3}$ , average diameters  $\langle d \rangle \sim 2.5 \text{ nm}$ , and volume fractions of  $\langle f \rangle \sim 0.45\%$  [19]. The smallest ( $d < 5 \text{ nm}$ ) NOs were found to be primarily Y<sub>2</sub>Ti<sub>2</sub>O<sub>7</sub>, while larger ( $d > 6 \text{ nm}$ ) NOs were primarily orthorhombic Y<sub>2</sub>TiO<sub>5</sub>. Larger ( $d > 50 \text{ nm}$ ) Y<sub>2</sub>O<sub>3</sub>, TiO<sub>x</sub>, Mo-rich, and C–N rich precipitates have also been observed. Unpublished x-ray diffraction (XRD) results also show the presence of TiO. Given the low volume fraction and ultra-small NO size, a synchrotron light source is needed to obtain reliable x-ray measurements. In this study, we performed a comprehensive x-ray absorption spectroscopy (XAS) analysis as a complement to XRD and SAXS measurements.

The wide variety of precipitate phases and sizes in NFAs complicates conventional XAS analysis. The many scattering environments cause significant overlap in spectrum features characteristic

of the individual phases. In the particular case of NFA MA957,  $\approx 2/3$  of the total Ti is left in solution and only  $1/3$  is contained in the various nano-oxides [20]. A previous XAS study by Liu et al. indicated nearly equal amounts of  $Y_2Ti_2O_7$ ,  $Y_2TiO_5$ , and  $Y_2O_3$  in MA957 [21].

In this study, we build on previous XAS work by using the log-ratio method to analyze the complex MA957 XAS spectra. We also detail a bulk extraction and selective filtration method to dissolve the alloy matrix and isolate one component of the NOs populations. We demonstrate that the filtration procedure not only yields samples that are geometrically ideal for XAS measurements, but also removes the problematic environments that hinder conventional analysis.

## 2. Material and methods

### 2.1. Materials

INCO NFA MA957 with a nominal composition of 14.9Cr, 1.1Ti, 0.17Mo, 0.13Y, 0.88O, bal. Fe (at%), along with trace impurity elements such as Al, Mn, Si and C [22] was examined in this study. The alloy was extruded at  $\sim 1060$  °C. XAS measurements were performed on the as-extruded MA957 alloy containing embedded NOs, and on filters containing extracted NOs.

### 2.2. Bulk extraction and filtration method

A bulk extraction and selective filtration method was used to isolate a NO population. The procedure is outlined in Fig. 1. MA957 was placed in a platinum wire mesh (Fig. 1a) and submerged into a 1 L solution composed of 100 mL acetyl acetone, 10 g of tetra methyl ammonium chloride, and a balance of methanol. A 20 V potential was used to dissolve the MA957 matrix. The non-acetic solution is

dark red at the end of the 24 h process (Fig. 1b). A 100 nm-pore filter was first used to remove very large particles (not shown in Fig. 1). The remaining liquid was drained through a polysulfone 10 nm-pore filter for 50 h. The process was accelerated by connecting a fume-hood vacuum to the filtration capsule (Fig. 1c). The filter containing NOs was used for XAS measurements (Fig. 1d). This procedure yields a roughly spatially uniform distribution of NOs in the filter, which is ideal for XAS studies.

### 2.3. XAS parameters

Both as-received MA957 alloy containing embedded NOs, and filters containing selectively extracted NOs, were studied using XAS fluorescence and transmission-mode measurements at beamline X23A2 of the National Synchrotron Light Source at Brookhaven National Laboratory. Ambient temperature XAS spectra were measured at the Ti and Y *K*-edges (4.492 keV and 17.038 keV, respectively), at a photoelectron wavenumber (*k*) value of  $13 \text{ \AA}^{-1}$ . Ti metal and  $Y_2O_3$  powder were simultaneously measured in transmission mode for energy calibration. Background subtraction, spectra alignment, and normalization of the extended x-ray absorption fine structure (EXAFS) data were carried out using the ATHENA code [23]. The positions of the Ti and Y edges were determined from the reference absorption spectra using known features. Isolated EXAFS spectra were then Fourier Transformed (FT) over a *k* range of  $3.0\text{--}11 \text{ \AA}^{-1}$  and back FT over a non-phase-corrected radial distance of  $0.9\text{--}2.4 \text{ \AA}$  to isolate the signal from the first nearest neighbor atoms (Ti–O and Y–O bonds).

Application of model-dependent analysis methods (using a combination of Artemis, IFEFFIT and FEFF) was found to be difficult due to structural disorder and weak signals present in the samples. Instead, structural parameters were determined using the model-independent, or log-ratio, method [24]. This purely empirical

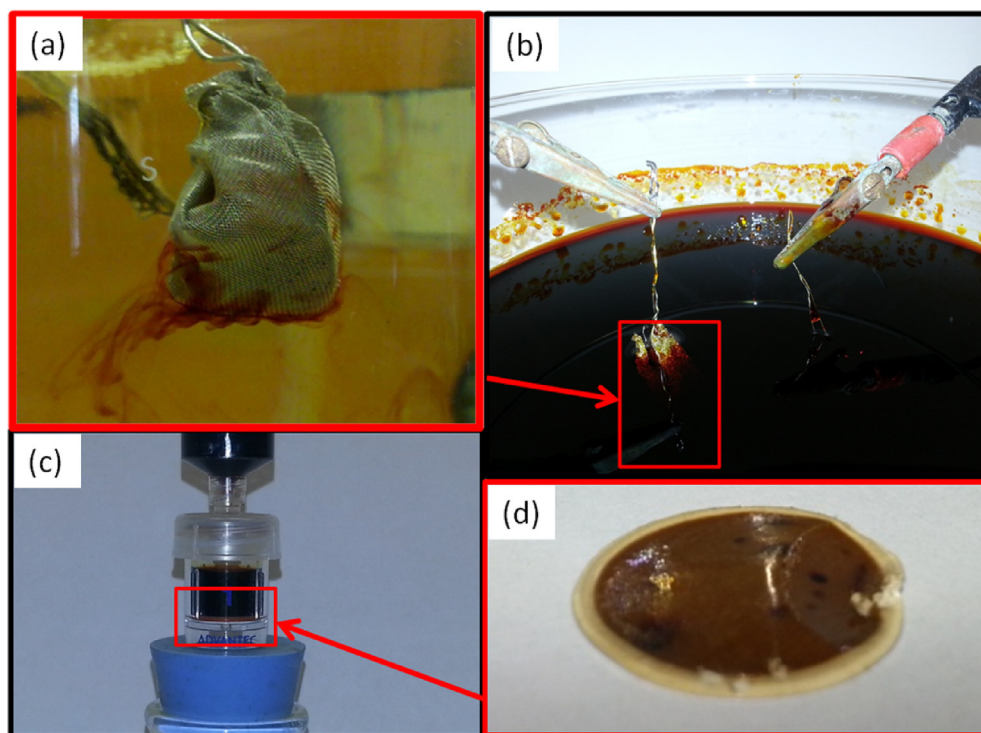


**Fig. 1.** (a) MA957 in platinum wire mesh being dissolved; (b) The initially clear yellow liquid is dark red at the end of the process; the liquid is then pre-treated by 100 nm-pore filtration (not shown); (c) a vacuum under a 10 nm-pore filter is used to accelerate the process; and, (d) the filter containing NOs is removed and used for XAS measurements. (For interpretation of the references to colour in this figure legend, the reader is referred to the web version of this article.)

technique is most useful for data where the signals from nearest neighbor (NN) atoms are spectrally isolated from the rest. The log-ratio method is commonly used to probe atomic changes with temperature/pressure, and has been used in both crystalline and amorphous materials [25]. Fitting of the log-ratio of amplitudes ( $\ln [A_{NO}(k)/A_S(k)]$ ) and phase-difference [ $\Phi_{NO}(k) - \Phi_S(k)$ ] of the isolated first NN atoms was performed using ATHENA over a  $k$  range of  $\sim 3$ – $8 \text{ \AA}^{-1}$  (depending on the edge) with polynomials of the forms shown in equations (1) and (2):

$$\frac{\Phi_{NO}(k) - \Phi_S(k)}{2k} = (BL_{NO} - BL_S) - \frac{4}{3}k^2(C_{3NO} - C_{3S}) \quad (1)$$

$$\ln\left(\frac{A_{NO}(k)}{A_S(k)}\right) = \ln\left(\frac{CN_{NO}}{CN_S}\right) - 2k^2(\sigma_{NO}^2 - \sigma_S^2) \quad (2)$$

The log-ratio technique yields differences in the structural parameters between the sample under investigation (subscript NO) and a known standard (subscript S). The reported differences in the bond length ( $\Delta BL = BL_{NO} - BL_S$ ), Debye – Waller factor ( $\Delta\sigma^2 = \sigma_{NO}^2 - \sigma_S^2$ ), asymmetry parameter ( $\Delta C_3 = C_{3NO} - C_{3S}$ ) and ratio of the coordination numbers ( $CN_{NO}/CN_S$ ) are relative to the bulk standards, and were allowed to vary. Further details of the log-ratio fitting are included in the [Supplementary section](#).

### 3. Results

#### 3.1. XANES

The XAS spectra are plotted as absorption versus x-ray energy, and consist of an x-ray absorption near edge structure (XANES) region with a broad edge and, in some cases, a pre-edge peak at lower energy, and an extended x-ray absorption fine structure (EXAFS) oscillating region at energies beyond the edge. The Ti and Y  $K$ -edge XANES spectra are shown in Fig. 2 for the embedded and extracted oxides, along with those for bulk standards. In Fig. 2, some curves have been vertically offset for clarity. The pre-edge peaks and broad features observed in the XANES spectra result from multiple-scattering resonances, and can be used to identify the crystallographic phase, symmetry and oxidation state of the metal ions [26,27]. At the Ti edge in Fig. 2a, the Ti atoms in the bulk MA957 (embedded) show a complex mixture of environments, similar to metallic Ti,  $Y_2Ti_2O_7$  and TiO. Note the higher intensity in the 4.99–5.02 keV range and subtle shifts relative to the bulk standards.

In contrast, the extracted NOs show a sharp pre-edge peak that is more characteristic of the  $Y_2TiO_5$  phase. Additionally, the general shape and the features in the edge ( $\sim 4.98$ – $5.0$  keV) are most similar to the  $Y_2TiO_5$  phase. The broad features in the XANES spectrum suggest structural disorder in the extracted NOs, likely due to their small size and complex chemistry. This observation is consistent with other nanoparticle studies, where changes in the XANES regions from structural and chemical disorder are reported [28].

The XANES spectra at the Y edge (Fig. 2b) show features for the embedded NOs that are almost identical to the  $Y_2Ti_2O_7$  standard. A small  $Y_2O_3$  component may also be present in the embedded measurement as indicated by a subtle increase in intensity between 17.05 – 17.07 keV and 17.10–17.12 keV, where  $Y_2O_3$  has similar XANES features.

The spectrum for the extracted NOs again shows very broad features that are more consistent with the  $Y_2TiO_5$  phase. Further, the features observed in the XANES Y edge for the extracted NOs are consistent with the Ti edge data and a disordered atomic environment.

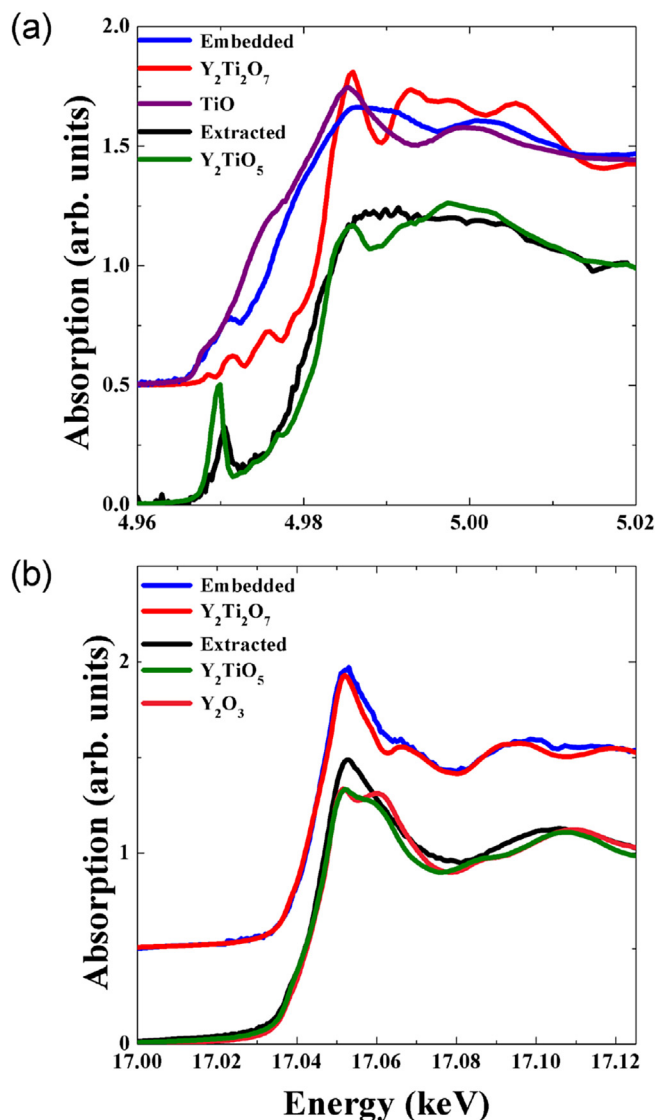
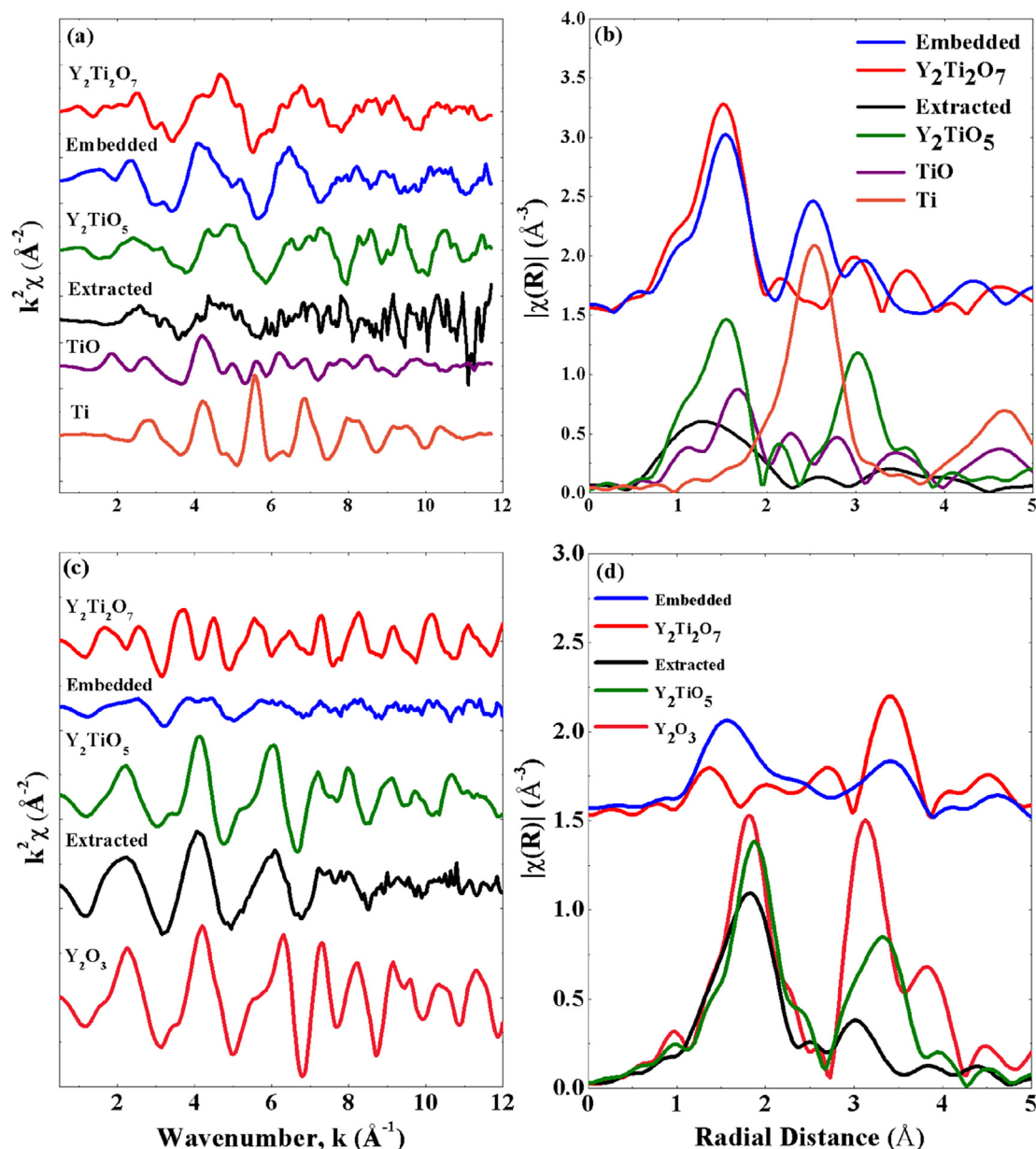


Fig. 2. XANES spectra at the  $K$ -edge for (a) Ti and (b) Y for the embedded and extracted measurements. The TiO,  $Y_2O_3$ ,  $Y_2TiO_5$  and  $Y_2Ti_2O_7$  bulk standards are shown for reference.

#### 3.2. EXAFS

The EXAFS spectra,  $k^2\chi(\text{\AA}^{-2})$ , and the magnitude of the Fourier Transformed spectra,  $|\chi(R)|(\text{\AA}^{-3})$ , for the Ti  $K$ -edge are shown in Fig. 3a and 3b, respectively, and for the Y  $K$ -edge in Fig. 3c and 3d, respectively. The different spectral features (oscillations in the  $k^2\chi$  and peaks in the  $|\chi(R)|$ ) result from single and multiple scattering from atoms around the absorbing atom of interest. The Ti  $K$ -edge EXAFS data for the as-received MA957 (embedded) is complex, with multiple environments giving rise to the observed fine structure. For example, the first peak at  $\sim 1.5 \text{ \AA}$  in the embedded spectrum is attributed to Ti–O bonds. The large intensity is indicative of multiple environments or bulk like structure. The second peak at  $\sim 2.5 \text{ \AA}$  is similar in position to the metallic Ti in solution. These features are consistent with previous studies where multiple Ti environments were also observed [21]. The extracted EXAFS show significantly less structure at the Ti edge, with a small peak at about  $1.25 \text{ \AA}$ , but overall weak signal beyond  $\sim 2 \text{ \AA}$ .

The Y  $K$ -edge EXAFS spectra (Fig. 3d) show that atomic



**Fig. 3.** EXAFS spectra  $k^2\chi(\text{\AA}^{-2})$  and the magnitude of the Fourier Transformed spectra,  $|\chi(R)|(\text{\AA}^{-3})$ , for the Ti K-edge are shown in (a) and (b), respectively, and for the Y K-edge in (c) and (d), respectively.

environments for the embedded NOs are complex with bond lengths of  $\sim 1.6$ ,  $2.4$  and  $3.4$  Å, similar to a mixture of the  $\text{Y}_2\text{Ti}_2\text{O}_7$ ,  $\text{Y}_2\text{O}_3$  and  $\text{Y}_2\text{TiO}_5$ . The extracted NOs again have a different structure, more closely resembling that of the  $\text{Y}_2\text{TiO}_5$  and  $\text{Y}_2\text{O}_3$  phases. The heights of the first peaks are, however, much lower in intensity compared to the standards potentially due to larger structural disorder and relatively small NO sizes.

### 3.3. Quantitative results

Table 1 shows the coordination number ratios ( $\text{CN}_{\text{NO}}/\text{CN}_{\text{S}}$ ), differences in bond length ( $\text{BL}_{\text{NO}}-\text{BL}_{\text{S}}$ ), differences in Debye – Waller factor ( $\sigma_{\text{NO}}^2-\sigma_{\text{S}}^2$ ), and differences in asymmetry parameter ( $\text{C}_{3\text{NO}}-\text{C}_{3\text{S}}$ ) between the nano-oxide and the standards. For each type of sample (embedded or extracted) and each edge (Ti or Y), the spectrum was analyzed relative to the two standards that most

resemble the observed spectral features from the XANES. For example, the Ti edge of the embedded spectrum most resembles the  $\text{Y}_2\text{Ti}_2\text{O}_7$  and  $\text{Y}_2\text{TiO}_5$  standards. Note that the embedded spectra have multiple Ti and Y environments and overlapping first nearest neighbor distances. Thus, the values for the embedded samples are an average of the multiple environments.

The Ti edge for the as-received MA957 (embedded) case have coordination number ratios close to 1. This value is considered large for nano-sized particles, and is likely due to the overlapping environments of the oxide phases. The changes in the Ti–O bond length (BL) were smaller for the  $\text{Y}_2\text{Ti}_2\text{O}_7$  phase than the  $\text{Y}_2\text{TiO}_5$  phase, consistent with the previous discussion.

The quantitative analysis of the embedded case at the Y edge indicates a mixture of the  $\text{Y}_2\text{O}_3$  and  $\text{Y}_2\text{Ti}_2\text{O}_7$  phases. However, the multiple overlapping environments hinder a full quantitative description of the structural parameters for both Ti and Y edges. As



**Table 1**  
Quantitative results from the EXAFS fitting indicating coordination number ( $CN_{NO}/CN_S$ ), bond length ( $\Delta BL$ ), Debye – Waller factor ( $\Delta\sigma^2$ ) and asymmetry parameter ( $\Delta C_3$ ). The subscripts NO and S are for nano-oxide and standard, respectively. \*The embedded sample has multiple Ti and Y environments, and overlapping first nearest neighbor distances. Thus, values are an average of the multiple environments.

Nano-oxide	Edge	Standard	$CN_{NO}/CN_S$	$(BL_{NO} - BL_S) \text{ \AA}$	$(\sigma^2_{NO} - \sigma^2_S) \times 10^{-3} \text{ \AA}^2$	$(C_{3NO} - C_{3S}) \times 10^{-4} \text{ \AA}^3$
Embedded*	Ti	$Y_2Ti_2O_7$	0.96 (0.07)	0.0924 (0.001)	3.69 (0.13)	3.7 (0.3)
Embedded*	Ti	$Y_2TiO_5$	1.10 (0.05)	0.156 (0.001)	3.56 (0.13)	11.8 (0.2)
Embedded*	Y	$Y_2TiO_5$	0.64 (0.02)	0.058 (0.002)	4.74 (0.62)	34.8 (0.4)
Embedded*	Y	$Y_2O_3$	0.65 (0.03)	0.083 (0.001)	5.42 (0.7)	31.8 (0.3)
Extracted	Ti	$Y_2TiO_5$	0.55 (0.04)	0.039 (0.003)	2.93 (0.047)	15.4 (0.6)
Extracted	Ti	TiO	0.60 (0.03)	0.076 (0.002)	2.46 (0.037)	13.1 (0.4)
Extracted	Y	$Y_2TiO_5$	0.87 (0.07)	−0.005 (0.001)	4.82 (0.36)	2.7 (0.2)
Extracted	Y	$Y_2O_3$	0.84 (0.06)	0.037 (0.001)	8.05 (0.29)	2.9 (0.2)

noted previously, the log-ratio method requires spectrally isolated nearest neighbor atoms.

The Ti *K*-edge quantitative results for the extracted NOs show a lower CN compared to the  $Y_2TiO_5$  and TiO standards. An increase in the  $\sigma^2$ , slight bond length expansion and increase in asymmetry are also observed. The extracted NO structural parameters at the Y edge show similar trends, with a decrease in the coordination number, subtle changes in bond length and increase in  $\sigma^2$ . A decrease in CN and increase in the  $\sigma^2$  are commonly observed in nanoparticle systems due to finite-size effects and large surface to volume ratios. These specifically include an increase in the number of under-coordinated surface atoms and relaxation/reconstruction of surface atoms away from their ideal positions. Additionally, the  $C_3$  is a measure of the asymmetric deviation from a Gaussian interatomic distance distribution and a positive value indicates that the BL distribution is skewed toward longer bond lengths. The positive  $\Delta C_3$  values for the extracted NO are potentially the result of surface atoms reconstructing away from the particle core. The results at both edges again indicate that the extracted NOs have a structure similar to  $Y_2TiO_5$  phase (albeit with slightly different CN, BL and  $\sigma^2$  due to finite size effects). All the structural changes in the extracted NO sample are consistent with the atomic environment commonly observed for other nanoparticle systems, where an increase in the surface-to-volume ratio results in an under-coordinated (low and reconstructed surface [28,29].

#### 4. Discussion

The Ti and Y *K*-edge environments were probed in both MA957 containing embedded NOs, and in filters containing extracted NOs. The broad first peak in the embedded case indicates that Ti is in multiple environments which include  $Y_2Ti_2O_7$ ,  $Y_2TiO_5$ , TiO, and metallic matrix Ti. Further, the Y spectrum is most consistent with  $Y_2Ti_2O_7$  and  $Y_2O_3$ . The  $Y_2TiO_5$  component of the Y-edge was nearly undetectable.

The bulk extraction and selective filtration procedure successfully captured the larger  $Y_2TiO_5$  particles (and perhaps others), and allowed a more discriminating analysis. The larger particles were trapped in the filters during extraction, while the smaller ones passed through. The Ti-edge spectrum from the extracted NOs had a pre-edge feature very similar to  $Y_2TiO_5$ . Further, the Y-edge features closely resemble those of  $Y_2TiO_5$  and  $Y_2O_3$ .

The use of the log-ratio method in this study, to quantify changes in NN bonding (Ti–O and Y–O bonds), is quite advantageous. The NN peaks for the extracted NOs are well isolated (no multiple scattering paths overlap) and correspond to common metal-oxygen bonds. Thus, quantitative analysis yields information on the structural state of the NOs relative to the bulk standards. Another advantage is that the log-ratio method does not assume any structure, thus the scattering amplitudes and phase shifts are not needed prior to analysis [30]. The combination of the

qualitative XANES and quantitative EXAFS results clearly demonstrate that the extraction process is capable of isolating a minor component that is essentially overwhelmed by the large and complex environment observed when the NOs are embedded in a matrix.

The authors are aware that the extraction process may affect the character of the NOs. For example, possible segregation of Ti, O, and Cr to NO interfaces cannot be observed by XAS since the matrix is dissolved during particle extraction. Further, the extracted NOs may partially restructure when they are released from the matrix. However, such extraction effects are not believed to be significant with respect to the core NOs, especially since they generally resemble those seen in TEM observations [11].

#### 5. Conclusions

In conclusion, the chemistries and structures of NOs in NFA MA957 were characterized by XAS for both embedded and extracted precipitates. The log-ratio method was used to successfully analyze the spectra and provide structural parameters relative to the known standards. Measurements on embedded NOs in bulk MA957 are most consistent with  $Y_2Ti_2O_7$ , while the slightly larger extracted oxides are primarily consistent with  $Y_2TiO_5$ . Analysis of the as-received MA957 was difficult due to the multiple Ti environments including  $Y_2Ti_2O_7$ ,  $Y_2TiO_5$ , TiO, and dissolved metallic Ti. The bulk extraction and selective filtration technique successfully removed the matrix, trapped the larger  $Y_2TiO_5$  particles, and yielded samples well suited for XAS measurements. The smaller  $Y_2Ti_2O_7$  oxides passed through the filters but were the predominant embedded phase. This will be further confirmed in the future by XAS measurements on the residues in the filter effluent. The described methods and analysis are an important complement to the other characterization techniques that have been applied to NFAs, a remarkable alloy system of rapidly growing worldwide interest, especially for advanced fission and fusion energy applications.

#### Acknowledgements

The authors thank Dr. Bruce Ravel for helping with beamline setup and data acquisition. This work was supported by the U.S. Department of Energy, Office of Fusion Energy Sciences, under grant DE-FG03-94ER54275. Use of the National Synchrotron Light Source, Brookhaven National Laboratory, was supported by the U.S. Department of Energy, Office of Science, Office of Basic Energy Sciences, under Contract Nos. DE-AC02-98CH10886 and DE-SC0012704.

#### Appendix A. Supplementary data

Supplementary data related to this article can be found at <http://dx.doi.org/10.1016/j.jallcom.2016.12.350>.

## References

- [1] G.R. Odette, Recent progress in developing and qualifying nanostructured ferritic alloys for advanced fission and fusion applications, *JOM* 66 (2014) 2427, <http://dx.doi.org/10.1007/s11837-014-1207-5>.
- [2] G.R. Odette, D.T. Hoelzer, Irradiation-tolerant nanostructured ferritic alloys: transforming helium from a liability to an asset, *JOM* 62 (2010) 84–92, <http://dx.doi.org/10.1007/s11837-010-0144-1>.
- [3] S.J. Zinkle, J.T. Busby, Structural materials for fission & fusion energy, *Mater. Today* 12 (2009) 12–19, [http://dx.doi.org/10.1016/S1369-7021\(09\)70294-9](http://dx.doi.org/10.1016/S1369-7021(09)70294-9).
- [4] N. Cunningham, Y. Wu, D. Klingensmith, G.R. Odette, On the remarkable thermal stability of nanostructured ferritic alloys, *Mater. Sci. Eng. A* 613 (2014) 296–305, <http://dx.doi.org/10.1016/j.msea.2014.06.097>.
- [5] N.J. Cunningham, Y. Wu, A. Etienne, E.M. Haney, G.R. Odette, E. Stergar, D.T. Hoelzer, Y.D. Kim, B.D. Wirth, S.A. Maloy, Effect of bulk oxygen on 14YWT nanostructured ferritic alloys, *J. Nucl. Mater.* 444 (2014) 35–38, <http://dx.doi.org/10.1016/j.jnucmat.2013.09.013>.
- [6] E.A. Marquis, Core/shell structures of oxygen-rich nanostructures in oxide-dispersion strengthened Fe-Cr alloys, *Appl. Phys. Lett.* 93 (2008) 10–13, <http://dx.doi.org/10.1063/1.3000965>.
- [7] C.A. Williams, P. Unifantowicz, N. Baluc, G.D.W. Smith, E.A. Marquis, The formation and evolution of oxide particles in oxide-dispersion-strengthened ferritic steels during processing, *Acta Mater.* 61 (2013) 2219–2235, <http://dx.doi.org/10.1016/j.actamat.2012.12.042>.
- [8] D.J. Larson, P.J. Maziasz, I.S. Kim, K. Miyahara, Three-dimensional atom probe observation of nanoscale titanium-oxygen clustering in an oxide-dispersion-strengthened Fe-12Cr-3W-0.4Ti + Y2O3 ferritic alloy, *Scr. Mater.* 44 (2001) 359–364, [http://dx.doi.org/10.1016/S1359-6462\(00\)00593-5](http://dx.doi.org/10.1016/S1359-6462(00)00593-5).
- [9] M.K. Miller, E.A. Kenik, K.F. Russell, L. Heatherly, D.T. Hoelzer, P.J. Maziasz, Atom probe tomography of nanoscale particles in ODS ferritic alloys, *Mater. Sci. Eng. A* 353 (2003) 140–145, [http://dx.doi.org/10.1016/S0921-5093\(02\)00680-9](http://dx.doi.org/10.1016/S0921-5093(02)00680-9).
- [10] Y. Wu, J. Ciston, S. Krämer, N. Bailey, G.R. Odette, P. Hosemann, The crystal structure, orientation relationships and interfaces of the nanoscale oxides in nanostructured ferritic alloys, *Acta Mater.* 111 (2016) 108–115, <http://dx.doi.org/10.1016/j.actamat.2016.03.031>.
- [11] Y. Wu, E.M. Haney, N.J. Cunningham, G.R. Odette, Transmission electron microscopy characterization of the nanostructures in nanostructured ferritic alloy MA957, *Acta Mater.* 60 (2012) 3456–3468, <http://dx.doi.org/10.1016/j.actamat.2012.03.012>.
- [12] J. Ribis, E. Borda, P. Trocellier, Y. Serruys, Y. de Carlan, A. Legris, Comparison of the neutron and ion irradiation response of nano-oxides in oxide dispersion strengthened materials, *J. Mater. Res.* 30 (2015) 2210–2221, <http://dx.doi.org/10.1557/jmr.2015.183>.
- [13] S.Y. Zhong, J. Ribis, N. Lochet, Y. de Carlan, V. Klosek, M.H. Mathon, Influence of nano-particle coherency degree on the coarsening resistivity of the nano-oxide particles of Fe-14Cr-1W ODS alloys, *J. Nucl. Mater.* 455 (2014) 618–623, <http://www.sciencedirect.com/science/article/pii/S002231151400573X>.
- [14] J. Ribis, Y. De Carlan, Interfacial strained structure and orientation relationships of the nanosized oxide particles deduced from elasticity-driven morphology in oxide dispersion strengthened materials, *Acta Mater.* 60 (2012) 238–252, <http://dx.doi.org/10.1016/j.actamat.2011.09.042>.
- [15] V. Badjeck, M.G. Walls, L. Chaffron, J. Malaplate, K. March, New insights into the chemical structure of Y2Ti2O7- $\delta$  nanoparticles in oxide dispersion-strengthened steels designed for sodium fast reactors by electron energy-loss spectroscopy, *J. Nucl. Mater.* 456 (2015) 292–301, <http://www.sciencedirect.com/science/article/pii/S0022311514006485>.
- [16] K. Dawson, G.J. Tatlock, Characterisation of nanosized oxides in ODM401 oxide dispersion strengthened steel, *J. Nucl. Mater.* 444 (2014) 252–260, <http://www.sciencedirect.com/science/article/pii/S0022311513011422>.
- [17] M. Ohnuma, J. Suzuki, S. Ohtsuka, S.-W. Kim, T. Kaito, M. Inoue, H. Kitazawa, A new method for the quantitative analysis of the scale and composition of nanosized oxide in 9Cr-ODS steel, *Acta Mater.* 57 (2009) 5571–5581, <http://dx.doi.org/10.1016/j.actamat.2009.07.054>.
- [18] M. Dumont, L. Commin, I. Morfin, F. DeGeuser, F. Legendre, P. Maugis, Chemical composition of nano-phases studied by anomalous small-angle X-ray scattering: application to oxide nano-particles in ODS steels, *Mater. Charact.* 87 (2014) 138–142, <http://dx.doi.org/10.1016/j.matchar.2013.11.008>.
- [19] N.J. Cunningham, Study of the Structure, Composition, and Stability of Y-Ti-O nm-Scale Features in Nano-structured Ferritic Alloys, University of California Santa Barbara, 2012.
- [20] M.J. Alinger, G.R. Odette, D.T. Hoelzer, On the role of alloy composition and processing parameters in nanocluster formation and dispersion strengthening in nanostructured ferritic alloys, *Acta Mater.* 57 (2009) 392–406, <http://dx.doi.org/10.1016/j.actamat.2008.09.025>.
- [21] S. Liu, G.R. Odette, C.U. Segre, Evidence for core-shell nanoclusters in oxygen dispersion strengthened steels measured using X-ray absorption spectroscopy, *J. Nucl. Mater.* 445 (2014) 50–56, <http://dx.doi.org/10.1016/j.jnucmat.2013.10.042>.
- [22] J.J. Fischer, Dispersion Strengthened Ferritic Alloy for Use in Liquid-metal Fast Breeder Reactors (LMFBRs), 1978, [http://www.iaea.org/inis/collection/NCLCollectionStore/\\_Public/09/394/9394580.pdf](http://www.iaea.org/inis/collection/NCLCollectionStore/_Public/09/394/9394580.pdf).
- [23] B. Ravel, M. Newville, ATHENA, ARTEMIS, HEPHAESTUS: data analysis for X-ray absorption spectroscopy using FEFFIT, *J. Synchrotron Radiat.* 12 (2005) 537–541, <http://dx.doi.org/10.1107/S0909049505012719>.
- [24] G. Bunker, Application of the ratio method of EXAFS analysis to disordered systems, *Nucl. Instrum. Methods Phys. Res.* 207 (1983) 437–444, [http://dx.doi.org/10.1016/0167-5087\(83\)90655-5](http://dx.doi.org/10.1016/0167-5087(83)90655-5).
- [25] P. Fornasini, S. a Beccara, G. Dalba, R. Grisenti, A. Sanson, M. Vaccari, F. Rocca, Extended x-ray-absorption fine-structure measurements of copper: local dynamics, anharmonicity, and thermal expansion, *Phys. Rev. B* 70 (2004) 174301, <http://dx.doi.org/10.1103/PhysRevB.70.174301>.
- [26] L.A. Grunes, Study of the K edges of 3d transition metals in pure and oxide form by x-ray-absorption spectroscopy, *Phys. Rev. B* 27 (1983) 2111–2131, <http://dx.doi.org/10.1103/PhysRevB.27.2111>.
- [27] F. Farges, G.E. Brown, J.J. Rehr, Ti K-edge XANES studies of Ti coordination and disorder in oxide compounds: comparison between theory and experiment, *Phys. Rev. B* 56 (1997) 1809–1819, <http://dx.doi.org/10.1103/PhysRevB.56.1809>.
- [28] L.L. Araujo, R. Giulian, D.J. Sprouster, C.S. Schnorr, D.J. Llewellyn, P. Kluth, D.J. Cookson, G.J. Foran, M.C. Ridgway, Size-dependent characterization of embedded Ge nanocrystals: structural and thermal properties, *Phys. Rev. B* 78 (2008) 94112, <http://dx.doi.org/10.1103/PhysRevB.78.094112>.
- [29] A.I. Frenkel, C.W. Hills, R.G. Nuzzo, A view from the inside: complexity in the atomic scale ordering of supported metal nanoparticles, *J. Phys. Chem. B* 105 (2001) 12689–12703, <http://dx.doi.org/10.1021/jp012769j>.
- [30] C.S. Schnorr, M.C.R. (Eds.), Springer Series in Optical Sciences 190 X-Ray Absorption Spectroscopy of Semiconductors, Springer, 2015, <http://dx.doi.org/10.1007/978-3-662-44362-0>.